Evaluating AISA + Hyperspectral Imager y for Mapping Black Mangr ove along the South Texas Gulf Coast

Chenghai Yang, James H. Everitt, Reginald S. Fletcher, Ryan R. Jensen, and Paul W. Mausel

Abstract

Mangrove wetlands are economically and ecologically important ecosystems and accurate assessment of these wetlands with remote sensing can assist in their management and conservation. This study was conducted to evaluate airborne AISA+ hyperspectral imagery and image transformation and classification techniques for mapping black mangrove populations on the south Texas Gulf coast. AISA+ hyperspectral imagery was acquired from two study sites and both minimum noise fraction (MNF) and inverse MNF transforms were performed. Four classification methods, including minimum distance, Mahalanobis distance, maximum likelihood, and spectral angle mapper (SAM), were applied to the noise-reduced hyperspectral imagery and to the band-reduced MNF imagery for distinguishing black mangrove from associated plant species and other cover types. Accuracy assessment showed that overall accuracy varied from 84 percent to 95 percent for site 1 and from 69 percent to 91 percent for site 2 among the eight classifications for each site. The MNF images provided similar or better classification results compared with the hyperspectral images among the four classifiers. Kappa analysis showed that there were no significant differences among the four classifiers with the MNF imagery, though maximum likelihood provided excellent overall and class accuracies for both sites. Producer's and user's accuracies for black mangrove were 91 percent and 94 percent, respectively, for site 1 and both 91 percent for site 2 based on maximum likelihood applied to the MNF imagery. These results indicate that airborne hyperspectral imagery combined with image transformation and classification techniques can be a useful tool for monitoring and mapping black mangrove distributions in coastal environments.

Introduction

Mangrove swamps are coastal wetlands characterized by salt-tolerant trees, shrubs, and other plants growing in intertidally inundated areas. Mangrove trees live on both sheltered coasts and inlands as well as along the bank of estuaries and rivers (Ramasubramanian *et al.*, 2006). Mangrove wetlands are found in tropical and subtropical regions of the world. In North America, they are found from the southern tip of Florida along the Gulf Coast to Texas. In the continental United States, only three species of mangrove grow: black mangrove [*Avicennia germinans* (L.) L.], red mangrove (*Rhizophora mangle* L.), and white mangrove [*Laguncularia racemosa* (L.) Gaertn. f.]. Black mangrove is the most common mangrove in the United States outside the Florida everglades (EPA, 2006).

Mangrove wetlands are regarded as economically and ecologically important ecosystems due to their intermediate position between the marine and terrestrial environments (Pasqualini *et al.*, 1999). They have high productivity of litter fall and woody biomass (Day *et al.*, 1987 and 1996), provide habitat and detritus food for fish and shellfish, and function as nurseries for a variety of fishes, prawns, and shellfishes (Sasekumar *et al.*, 1992; Primavera, 1997). Moreover, mangrove forests provide a natural barrier that helps to prevent shoreline erosion, shielding inland areas from severe damage during hurricanes and tidal waves (Marshal, 1994; EPA, 2006). They also act as a windbreak, prevent salinization of soils, and filter pollutants (Tam and Wong, 1999; Mao *et al.*, 2006).

Valiela *et al.* (2001) estimated from their compilation of most recent data for all countries where mangroves have been reported, that there are roughly 17 million hectares of mangrove habitats along the shorelines of the world. Although mangrove wetlands are one of the most productive ecosystems and provide large amounts of resources, they are being increasingly cleared for other land-use activities such as settlements, agriculture, and aquaculture. On a worldwide scale, mangroves have been lost each year since the early-1980s with an annual areal loss rate of 2.1 percent, which exceeds the losses for tropical rain forests and coral reefs, two other well-known threatened environments. On a continental basis, losses vary and the largest losses occur in the Americas with an annual loss rate of 3.6 percent (Valiela *et al.*, 2001).

Efforts are needed to protect and restore these valuable ecosystems. To formulate effective management and

Chenghai Yang, James H. Everitt, and Reginald S. Fletcher are with the USDA-ARS Kika de la Garza Subtropical Agricultural Research Center, 2413 E. Highway 83, Weslaco, TX 78596 (chenghai.yang@ars.usda.gov).

Ryan R. Jensen and Paul W. Mausel are with the Department of Geography, Geology, and Anthropology, Indiana State University, Terre Haute, IN 47809.

Photogrammetric Engineering & Remote Sensing
Vol. 75, No. 4, April 2009, pp. 425–435.

0099-1112/09/7504–0425/$3.00/0

conservation plans and practices, it is very important to understand the compositions and distributions of plant communities in mangrove wetlands. Because of their inaccessibility and large extent, remote sensing can provide a cost-effective tool to monitor and map the distribution and dynamics of these plant communities. Traditional satellite multispectral imagery such as Landsat and SPOT has been used for mapping mangroves and assessing their overall conditions on a regional basis (Jensen *et al.*, 1991; Gang and Agatsiva, 1992; Long and Skewes, 1996; Ramsey and Jensen, 1996; Green *et al.*, 1998; Seto and Fragkias, 2007). Some studies have employed a combination of two or more these types of satellite imagery. Gao (1999) used SPOT multispectral (XS) and Landsat Thematic Mapper (TM) imagery for mapping mangroves in a temperate zone in New Zealand. Satito *et al.* (2003) evaluated SPOT-4 High Resolution Visible and Infrared (HRVIR) and Terra Advanced Spaceborne Thermal Emission and Reflection Radiometer (ASTER) data for mapping mangroves and related coastal ecosystems in the Arabian Gulf. Vaiphasa *et al.* (2006) integrated soil pH data into the mapping process to improve the accuracy of mangrove maps classified from ASTER imagery. Ramasubramanian *et al.* (2006) used Landsat TM and Indian Remote Sensing Satellite (IRS) LISS-III images to understand the changes in the extent of mangroves in an estuary in India between 1986 and 2001. Kumar *et al.* (2007) also used IRS LISS-III data to study the cover change in major coastal vegetation, including mangroves, in Sagar Island, India.

Aschbacher *et al.* (1995) employed both optical and microwave satellite data to evaluate their performance for mapping mangrove vegetation. The optical data included Landsat TM, SPOT XS, and Marine Observing Satellite (MOS) Multispectral Electronic Self-Scanning Radiometer (MESSR) imagery. The microwave or radar data were from the First European Remote Sensing Satellite (ERS-1) sensor and the Japanese Earth Resources Satellite (JERS-1) Synthetic Aperture Radar (SAR), both of which enable image acquisition under any weather condition and at any time of the day. They found that radar imagery alone can not discriminate mangrove and non-mangrove, but when it is combined with SPOT XS data, it offers an additional dimension in identifying trees of varying heights or groups of mangrove tree species with uniform heights. Pasqualini *et al.* (1999) also used SPOT XS and ERS-1 radar data for mangrove mapping.

Although conventional satellite systems play an important role in mapping mangrove distributions over large geographic regions, their relatively low spatial resolutions may have compromised the classification results for areas with small patches of mangrove stands or for areas with multiple mangrove species and similar plant species. Aerial photography and airborne video imagery have fine spatial resolution and are useful remote sensing techniques for mapping mangrove communities. Aerial color-infrared (CIR) photography, CIR videography, and false color digital imagery with visible/near-infrared (NIR)/mid-infrared sensitivity have been evaluated to distinguish black mangrove populations on the Texas Gulf coast (Everitt and Judd, 1989; Everitt *et al.*, 1991, 1999, and 2007). Aerial photographs have been used in many other studies to derive vegetation maps of mangrove forests (Chauvaud *et al.*, 1998; Kairo *et al.*, 2002; Verheyden *et al.*, 2002), to assess the changes in the distribution and extent of mangroves within Moreton Bay, southeast Queensland, Australia (Manson *et al.*, 2003), and to study the changes in the spatial extent of the impact of shrimp pond wastes on mangrove forest development in Pak Phanang, Thailand along with Landsat images (Vaiphasa *et al.*, 2007).

The availability of high-resolution satellite imagery such as Ikonos and QuickBird has opened up new opportunities for mapping mangrove communities. Wang *et al.* (2004a and 2004b) used Ikonos and QuickBird satellite imagery in conjunction with different image processing techniques to distinguish three mangrove species (black, red, and white mangroves) on the Caribbean coast of Panama. These studies indicated that both types of images had promising results in separating mangrove species. Proisy *et al.* (2007) assessed the potential of Fourier-based textural ordination to estimate mangrove forest biomass from Ikonos images.

Hyperspectral remote sensing provides tens to hundreds of spectral bands and has the potential for better differentiation of mangrove communities. Green *et al.* (1998) employed Compact Airborne Spectrographic Imager (CASI) hyperspectral data as well as Landsat TM and SPOT multispectral data for separating mangroves. Their results indicated that the satellite data failed to discriminate mangrove vegetation satisfactorily, but the CASI data provided higher classification accuracy and could separate more mangrove classes. Held *et al.* (2003) explored the possibility of combining CASI hyperspectral data with airborne radar data for mapping and monitoring of mangrove estuaries in far North Queensland, Australia. Classifications of both the individual and integrated datasets were performed with the latter producing more accurate results. Hirano *et al.* (2003) used Airborne Visible/Infrared Imaging Spectrometer (AVIRIS) data with 224 bands and 20 m spatial resolution to produce a vegetation map for a portion of Everglades National Park in Florida. The Everglades vegetation communities, including mangrove species, were satisfactorily identified. Errors in the classification map are partially due to the relatively coarse spatial resolution of the image data. Vaiphasa *et al.* (2005) used spectra of crown canopy leaves of 16 Thai tropical mangrove species measured using a spectrometer under laboratory conditions to discriminate the mangrove species and found that the 16 mangrove species were statistically different at most spectral locations.

Although a variety of spaceborne and airborne imagery has been used for mapping mangrove wetlands, the use of hyperspectral imagery for mangrove discrimination is still very limited. The increasing availability of hyperspectral data is generally expected to enhance wetland mapping capability, but the potential of this type of data for mapping wetland vegetation has not been fully demonstrated. The objective of this study was to evaluate airborne AISA+ hyperspectral imagery and image transformation and classification techniques for mapping black mangrove populations on the south Texas Gulf coast.

Methods

Study Area

This study was conducted in South Padre Island, Texas, which is located on the tropical southern tip of Texas just 40 km north of the Mexican border. The island is bordered to the east by the Gulf of Mexico and to the west by the Laguna Madre bay. The 55 km long sandy beaches of South Padre are known throughout the United States and draw thousands of visitors to the area each year. Black mangrove grows on the island and the nearby bay area. Two black mangrove sites on the west coast of the island, designated as sites 1 and 2, were selected for this study. The geographic coordinates near the centers of the sites are (97°10′05″ W, 26°04′59″ N) for site 1 and (97°10′29″ W, 26°08′11″ N) for site 2. Black mangrove was the dominant vegetation at site 1, while dense stands of cattail (*Typha domingensis* Pers.) occurred adjacent to the mangrove populations at site 2. Other plant species found in the study area included smooth cordgrass (*spartina alterniflora* Lois.), salt-marsh

bulrush (*Scripus maritimus* L.), bushy bluestem [*Andropogon glomeratus* (Walt.) B. S. P.], maritime saltwort (*Batis maritima* L.), shoregrass (*Monanthochloe littoralis* Engelm.), Texas sabal palm [*Sabal texana* (O.F. Cook) Becc.], natal plum [*Carissa grandiflora* A. DC.], and sea grape [*Coccoloba uvifera* (L.) L.]. Black mangrove trees in the study area were rarely over 3 m tall and most stands had a height of 1.5 to 2 m. They generally grew along the west coast of the island with strips ranging from a few meters to over 200 m wide, though smaller stands also existed within the study area.

Airborne Hyperspectral Image Acquisition

An AISA+ airborne hyperspectral imaging system was used to acquire images from the two study sites. AISA+ was a pushbroom imaging system consisting of a hyperspectral sensor head, a miniature Global Positioning System/Inertial Navigation System (GPS/INS) unit, and a rugged data acquisition PC with a display. The imaging system was capable of collecting 12-bit images with up to 248 spectral bands in a spectral range of 392 to 965 nm. For this study, the system was configured to collect 248 spectral bands with a swath of 512 pixels.

A Cessna 404 twin-engine aircraft with a camera port in the floor was used as the platform for image acquisition. The hyperspectral imaging system was mounted over the camera port using a light aluminum frame. The aircraft was stabilized at a predetermined altitude of 1520 m (5,000 ft) above ground level, a speed of 278 km/h (173 mi/h), and a straight-line flight direction before the start of image acquisition, and was maintained at the same altitude, speed, and direction during the course of image acquisition for each site. Hyperspectral images were acquired from the two sites on 23 May 2006 between 1830 and 1930h UTC under sunny and calm conditions. A square ground pixel size of 2.1 m was achieved.

For radiometric calibration, four 8 m by 8 m tarpaulins with nominal reflectance values of 4, 16, 32, and 48 percent, respectively, were placed in the study area during image acquisition. The actual reflectance values from the tarpaulins were measured using a FieldSpec HandHeld spectroradiometer (Analytical Spectral Devices, Inc., Boulder, Colorado) at the same time of the image acquisition. The spectroradiometer was sensitive in the visible to NIR portion of the spectrum (325 to 1,075 nm) with a spectral sampling interval of 1 nm. The spectroradiometer had a field of view angle of 25° and was held at 1 m above the tarpaulins during data collection.

Image Processing and Analysis

The GPS/INS data recorded during image acquisition were not used for geometric correction because of incomplete GPS data. Therefore, roads appearing in the images were used as a reference for the correction. Some curved roads existed in the image for site 1 and a straight road appeared in the image for site 2. The straight road approximately parallel to the flight line at site 2 was first overlaid on the corresponding distorted line in the raw image. Then, the distances in pixels between the reference line and the distorted line were determined for each row of the raw image. Finally, each row was shifted in the across-track direction by the number of pixels determined. For the geometric restoration of the image for site 1, a curved road approximately along the flight direction was first identified in the raw image and a rectified aerial CIR photo covering the hyperspectral image area was used as the reference image. The curved road in the aerial photo was digitized, rescaled, and overlaid on the distorted road in the raw hyperspectral image. The rest of the procedure was similar to the reference line approach used for site 2. Computer programs were written to perform the geometric corrections.

The geometrically restored hyperspectral images for the two sites were rectified to two respective georeferenced CIR photographs. The photographs were taken along with the hyperspectral imagery and then digitized and rectified to the Universal Transverse Mercator (UTM) coordinate system based on a set of the ground control points located with a sub-meter accuracy GPS Pathfinder Pro XRS receiver (Trimble Navigation Limited, Sunnyvale, California). The rectified photographic images had a pixel size of 0.5 m and a root mean square error (RMSE) error of 1.3 m for site 1 and 1.0 m for site 2. Due to the nonlinear nature of the distortions in the hyperspectral images, 93 points for site 1 and 116 points for site 2 were identified evenly throughout both the aerial photographic images and hyperspectral images and rubber sheeting techniques were used to rectify the hyperspectral images. The rectified hyperspectral images were converted to reflectance based on 248 empirical line calibration equations (one for each band) relating the actual reflectance values to the digital count values on the four tarpaulins. All procedures for image rectification and calibration were performed using ERDAS Imagine© (Leica Geosystems Geospatial Imaging, LLC, Norcross, Georgia). Because the camera had low quantum efficiency near the NIR end of the observed spectrum, the reflectance values for wavelengths greater than 924 nm were not reliable. In addition, the first 16 bands in the blue region appeared to be noisy. Therefore, bands 1 through 16 and 231 through 248 (a total of 34 bands) were removed from each hyperspectral image, and the remaining 214 bands with center wavelengths of 427 nm to 922 nm were used for analysis.

The minimum noise fraction (MNF) transformation implemented in ENVI (Research Systems, Inc., Boulder, Colorado) was used to reduce the high spectral dimensionality and inherent spectral noise in the hyperspectral imagery. The MNF transform is based on two principal components analysis (PCA) transformations and divides the original hyperspectral data into two parts: one part associated with large eigenvalues and coherent eigenimages, and a complementary part with near-unity eigenvalues and noise-dominated images (Green *et al.*, 1988; Boardman and Kruse, 1994). By using the smaller number of coherent eigenimages, the computational time and complexity for image analysis are reduced and, more importantly, the noise is separated from the data, thus improving spectral processing results. After the MNF procedure was applied to the 214-band hyperspectral images, coherent eigenimages were identified from all the MNF band images. Then an inverse MNF transformation was used to transform the coherent eigenimages to noise-reduced 214-band hyperspectral images.

Supervised classification techniques were employed to classify the two noise-reduced hyperspectral images and the two coherent MNF images using ENVI. The two sites had different cover types. The classes for site 1 consisted of black mangrove, mixed herbaceous, and woody species, wet and dry soil, paved roads, and water. The classes for site 2 were black mangrove, cattail, mixed herbaceous species, algae flats, bare soil, and water. Because of the variations within the classes, most of the major classes were divided into two or more subclasses. For site 1, there were two black mangrove subclasses, two mixed herbaceous subclasses, one mixed woody class, two soil subclasses, one pavement class, and two water classes. For site 2, there were two black mangrove subclasses, two cattail subclasses, four mixed herbaceous subclasses, two algae subclasses, two soil subclasses, and two water subclasses. Thus, there were a total of 10 classes for site 1 and a total of 14 classes for site 2. For supervised training, differing numbers of areas, or regions of interest, with known cover types were selected and digitized on each image as the training samples to

represent respective classes or endmembers. The numbers of digitized training pixels ranged from 504 to 1,391 among the classes for site 1 and from 507 to 1,009 for site 2. A boundary was defined for each site to exclude the areas outside the boundary for image classification.

Four supervised classification methods, including minimum distance, Mahalanobis distance, maximum likelihood, and spectral angle mapper (SAM), were applied to the noise-reduced hyperspectral images and the transformed coherent MNF images. The minimum distance classifier uses the class means derived from the training data and assigns each pixel to the class that has the closest Euclidean distance from the pixel (Campbell, 2002). The Mahalanobis distance method is similar to minimum distance, except that the covariance matrix is used in the calculation (ERDAS, 2002). Each pixel is assigned to the class for which Mahalanobis distance is the smallest. Maximum likelihood classification assumes that the data for each class in each band are normally distributed, and it calculates the probability that a given pixel belongs to a specific class (Richards, 1999). Each pixel is assigned to the class that has the highest probability (i.e., the maximum likelihood). Spectral angle mapper or SAM is a spectral classification technique that uses the *n*-dimensional angle to match pixels to endmembers (Kruse *et al.*, 1993). The algorithm determines the spectral similarity between a pixel spectrum and an endmember spectrum by calculating the angle between them, treating them as vectors in a space with dimensionality equal to the number of bands. Each pixel is assigned to the endmember whose spectrum has the smallest spectral angle with the pixel spectrum.

The classification maps resulting from the four classifiers contained 10 classes for site 1 and 14 classes for site 2. These classes were then merged into the five defined major classes for site 1 and the six major classes for site 2. For accuracy assessment of the merged classification maps for sites 1 and 2, 150 points were generated and assigned to the classes in a stratified random pattern for each site. The UTM coordinates of these points were determined and the Pathfinder Pro XRS GPS receiver was used to navigate to these points for ground verification. Error matrices for each classification map were generated by comparing the classified classes with the actual classes at these points. Classification accuracy measures including overall accuracy, producer's accuracy, user's accuracy, and kappa coefficients were calculated based on the error matrices (Congalton and Green, 1999). Kappa analysis was also performed to test if each classification was significantly better than a random classification and if any two classifications were significantly different. The test statistic for testing the significance of a single classification was a standardized *Z*-value calculated from the overall kappa value and kappa variance for the classification, and the test statistic for testing the difference between any two classifications was also a standardized *Z*-value determined from the difference between the kappa values and the sum of the kappa variances for the two classifications (Congalton and Green, 1999). Two-tailed *Z* tests were performed to determine if $Z > Z_{0.025}$ at the 95 percent confidence level.

Results and Discussion

Plate 1 shows CIR composites derived from the geometrically corrected hyperspectral images for sites 1 and 2. The distortion in the raw images can be seen from the curved edges of the CIR images. Although the CIR images display only three of the 214 bands in the hyperspectral images, they reveal distinct spatial patterns of different plant species and other cover types at each site. Black mangrove occurred along the west coast of the island at both sites, though it was more abundant at site 1 than at site 2. There was only a narrow strip of black mangrove along the west coast on the lower portion of site 2, and some mangrove stands also occurred between and around the ponds near the middle of the site. Cattail occupied the upper left portion of site 2 and a narrow strip of smooth cordgrass was found along the west coast next to cattail. In the CIR images, black mangrove had a reddish color, compared with the bright red response of ornamental trees enclosed by the paved roads at site 1. Cattail also had a reddish response, and it appeared brighter than black mangrove in the image. The brighter red responses of the ornamental trees and cattail on the CIR images were due to their higher NIR reflectance. Mixed herbaceous vegetation had a dull red to gray-reddish response in the images, while algae flats had a gray to grayish-brown response. Bare soil had a dark to light gray image color and paved roads appeared dark grayish in the images. Water had a blue image tone along the west coast, but had a dark blue response in the ponds because water in the ponds was calm and clear.

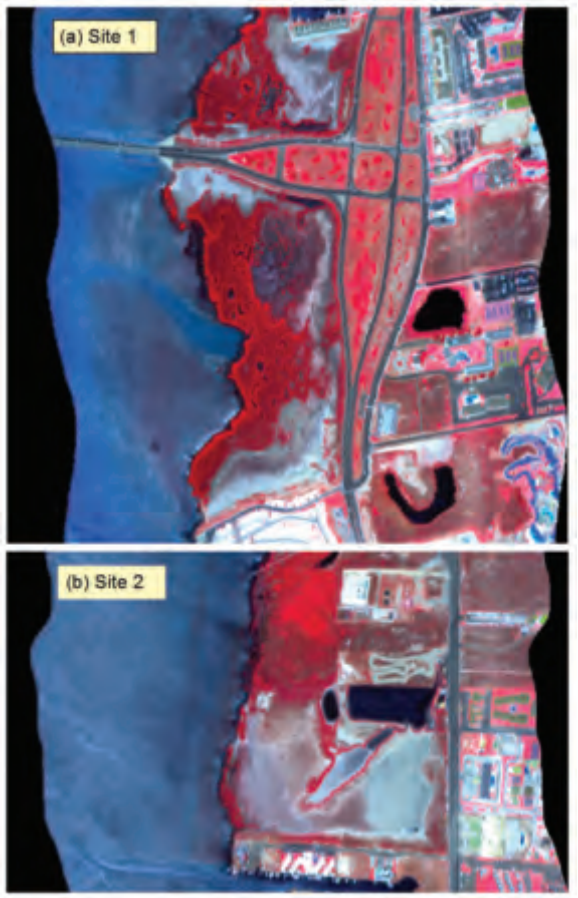

Plate 1. Color-infrared (CIR) images of two mangrove swamps on the south Texas Gulf coast: (a) Site 1, and (b) Site 2. The CIR images were extracted from the geometrically corrected AISA + hyperspectral images for sites 1 and 2, respectively. The center wavelengths for the near-infrared, red, and green bands were 820, 673, 530 nm, respectively, and the bandwidth was 2.3 nm.

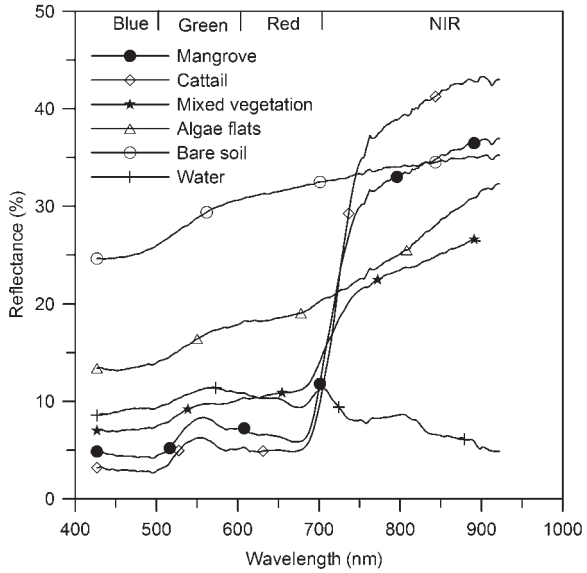

Figure 1. Representative reflectance spectra of black mangrove and associated cover types extracted from an AISA + 214-band hyperspectral image of a mangrove swamp (Site 2) on the south Texas Gulf coast.

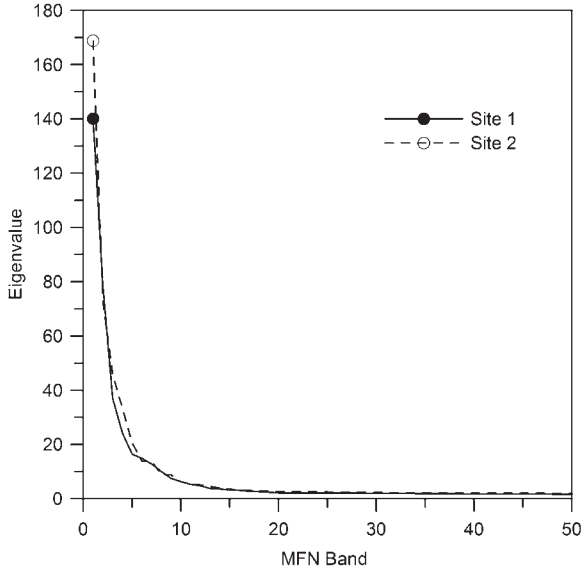

Figure 2. Minimum noise fraction (MNF) eigenvalues versus MNF bands derived from the original 214-band hyperspectral images for two black mangrove swamps (Sites 1 and 2) on the south Texas Gulf coast. Bands with large eigenvalues contain useful data, and bands with eigenvalues near one contain noise.

Figure 1 shows representative reflectance spectra for black mangrove, cattail, mixed vegetation, algae flats, bare soil, and water extracted from the 214-band hyperspectral image for site 2. Each spectrum represents the average of a number of pixel spectra extracted from each of the known cover types. Cattail had the lowest visible reflectance and the highest NIR reflectance among the six major classes. Black mangrove had lower visible reflectance than mixed vegetation and other cover types and higher NIR reflectance than mixed vegetation, algae flats, and water. Algae flats had higher visible reflectance than the three vegetation classes, while bare soil had the highest visible reflectance. Water had the lowest NIR reflectance, even though it had higher visible reflectance than the vegetation classes because of the turbidity and waves along the coast. Although each major class cannot be described by one single reflectance spectrum because of the within-class variations, the spectral characteristics shown in Figure 1 indicate that black mangrove can be spectrally distinguished from the other cover types.

Figure 2 shows eigenvalues of the first 50 MNF bands versus MNF band numbers for the two sites. Eigenvalues decrease sharply from 140 for site 1 and from 170 for site 2 to a near-constant value of 2 after band 20. Since bands with large eigenvalues contain useful data and bands with eigenvalues near one contains noise, the bands greater than 20 contain essentially noise. Based on the eigenvalue plots and visual inspection of the MNF band images, the first 20 bands from the transformed MNF images were selected as the useful and spatially coherent bands for inverse transformation and image classification.

Plate 2 shows a 10-class classification map from the noise-reduced 214-band hyperspectral image and a 10-class classification map from the 20-band MNF image based on maximum likelihood for site 1. The merged five-class maps for the respective images are also shown in the plate. Similarly, Plate 3 shows a 14-class classification map derived from the 214-band hyperspectral image and a 14-class classification map from the 20-band MNF image based on maximum likelihood as well as the merged six-class maps for site 2. A visual comparison of the classification maps with the CIR images indicates that the cover types at each site were generally well separated on these classification maps.

Table 1 summarizes the accuracy assessment results for the classification maps generated from both the 214-band hyperspectral image and the 20-band MNF image based on the four classification methods for site 1. Overall accuracy ranged from 84 percent based on SAM to 95 percent based on Mahalanobis distance and maximum likelihood for the hyperspectral image and from 91 percent based on SAM to 95 percent based on maximum likelihood for the 20-band MNF image. Overall kappa varied from 0.79 to 0.93 for the hyperspectral image and from 0.89 to 0.93 for the MNF image among the four classification methods. All the classifications were significantly better than a random classification at the 95 percent confidence level.

Table 2 presents *Z*-statistic values for making pairwise comparisons among the eight classifications for site 1. Mahalanobis distance and maximum likelihood were significantly better than minimum distance and SAM with the 214-band hyperspectral image, but there were no significant differences between Mahalanobis distance and maximum likelihood or between minimum distance and SAM with the hyperspectral image. There were no significant differences among the four classifications with the 20-band MNF image. The classifications from the MNF image based on Mahalanobis distance and maximum likelihood were significantly better than those from the hyperspectral image based on minimum distance and SAM. Moreover, the minimum distance-based classification from the MNF image was also significantly better than SAM-based classification from the hyperspectral image. These results indicate that the transformed MNF image was more effective than the 214-band

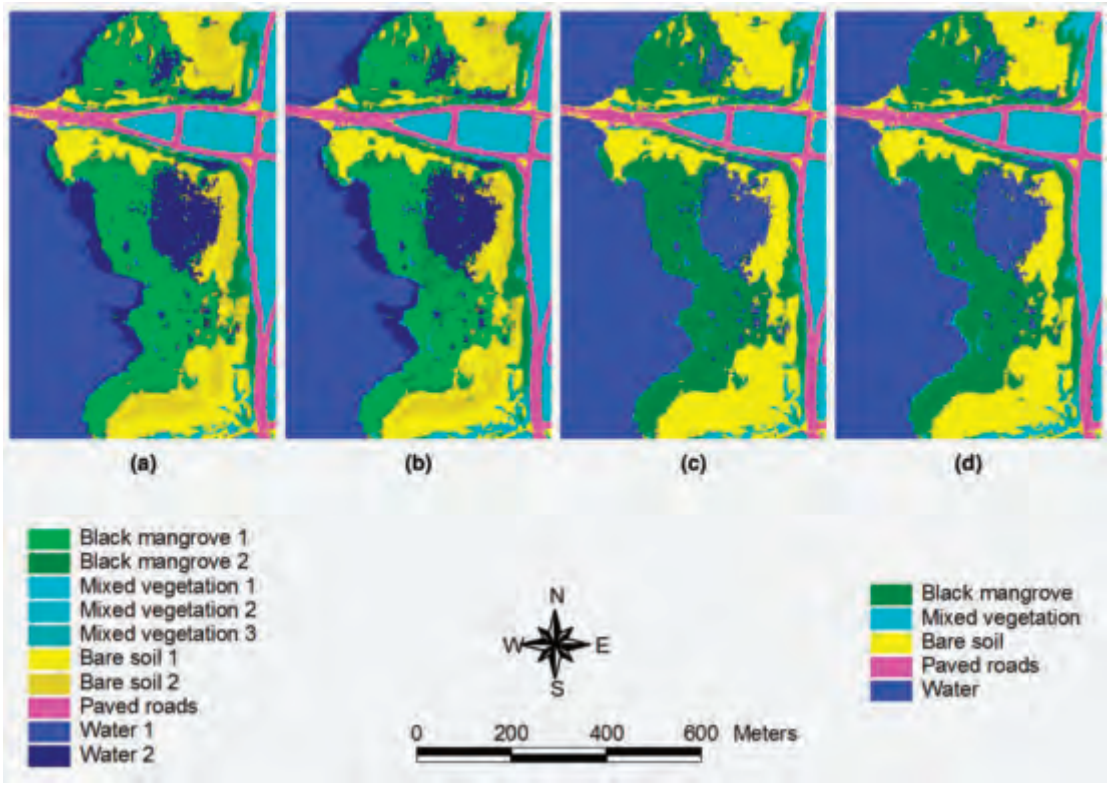

Plate 2. Maximum likelihood classification maps for a mangrove swamp on the south Texas Gulf coast (Site 1): (a) 10-class map based on 214-band hyperspectral image, (b) 10-class map based on 20-band MNF image, (c) Merged 5-class map based on 214-band hyperspectral image, and (d) Merged 5-class map based on 20-band MNF image.

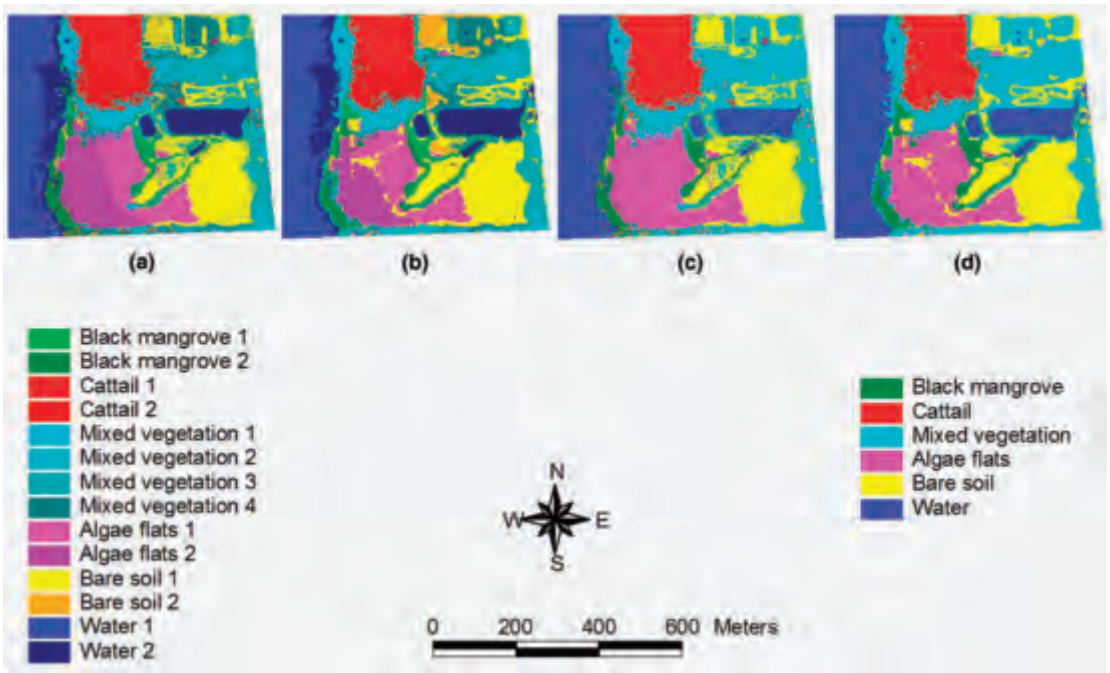

Plate 3. Maximum likelihood classification maps for a mangrove swamp on the south Texas Gulf coast (Site 2): 14-class map based on 214-band hyperspectral image, (b) 14-class map based on 20-band MNF image, (c) Merged 6-class map based on 214-band hyperspectral image, and (d) Merged 6-class map based on 20-band MNF image.

TABLE 1. ACCURACY ASSESSMENT RESULTS FOR EIGHT CLASSIFICATION MAPS GENERATED FROM A NOISE-REDUCED 214-BAND HYPERSPECTRAL IMAGE AND ITS 20-BAND MINIMUM NOISE FRACTION (MNF) IMAGE FOR A MANGROVE SWAMP ON THE SOUTH TEXAS GULF COAST (SITE 1)

Classification method	Overall accuracy (%)	Overall kappa	*Z* statistic	Producer's accuracy (PA, %) and user's accuracy (UA, %)									
				Black mangrove		Mixed vegetation		Bare soil		Paved roads		Water	
				PA	UA	PA	UA	PA	UA	PA	UA	PA	UA
214-band hyperspectral image													
MD[a]	86.7	0.829	23.57*	81.8	96.4	89.3	83.3	92.9	76.5	66.7	71.4	91.3	95.5
MAHD	94.7	0.931	39.42*	87.9	96.7	92.9	96.3	96.4	90.0	93.3	100.0	100.0	93.9
ML	94.7	0.931	39.39*	90.9	93.8	89.3	96.2	96.4	93.1	93.3	100.0	100.0	93.9
SAM	84.0	0.794	20.83*	78.8	74.3	60.7	70.8	96.4	79.4	80.0	100.0	95.7	97.8
20-band MNF image													
MD	93.3	0.914	34.87*	90.9	96.8	92.9	96.3	85.7	96.0	93.3	87.5	100.0	90.2
MAHD	94.0	0.923	37.01*	87.9	93.5	89.3	96.2	96.4	93.1	93.3	93.3	100.0	93.9
ML	94.7	0.931	39.39*	90.9	93.8	89.3	96.2	96.4	93.1	93.3	100.0	100.0	93.9
SAM	91.3	0.888	30.00*	84.8	96.6	92.9	92.9	82.1	95.8	93.3	87.5	100.0	86.8

[a] MD = minimum distance, MAHD = Mahalanobis distance, ML = maximum likelihood, and SAM = spectral angle mapper.
* Significantly different from a random classification at the 0.05 level. The critical value $Z_{0.025}$ is 1.96.

TABLE 2. KAPPA ANALYSIS RESULTS (Z-STATISTIC) FOR PAIRWISE COMPARISONS AMONG EIGHT CLASSIFICATION MAPS GENERATED FROM A 214-BAND HYPERSPECTRAL IMAGE AND ITS 20-BAND MNF IMAGE FOR A MANGROVE SWAMP ON THE SOUTH TEXAS GULF COAST (SITE 1)

Classification method	Based on 214-band hyperspectral image				Based on 20-band MNF image		
	MD	MAHD	ML	SAM	MD	MAHD	ML
Original image							
MAHD[a]	−2.41*						
ML	−2.41*	0.00					
SAM	0.68	3.06*	3.06*				
MNF image							
MD	−1.94	0.49	0.49	−2.59*			
MAHD	−2.17*	0.25	0.25	−2.83*	−0.24		
ML	−2.41*	0.00	0.00	−3.06*	−0.49	−0.25	
SAM	−1.28	1.14	1.14	−1.95	0.66	0.90	1.14

[a] MD = minimum distance, MAHD = Mahalanobis distance, ML = maximum likelihood, and SAM = spectral angle mapper.
* Significantly different from a random classification at the 0.05 level. The critical value $Z_{0.025}$ is 1.96. The negative sign indicates that the classification method on the top is worse than the one on the left.

hyperspectral image. Another advantage of using the MNF image was the reduction in computation time for image classification.

Producer's accuracy and user's accuracy are more meaningful measures for individual classes. Producer's accuracy of a class indicates the probability of actual areas for that class being correctly classified, and user's accuracy of a class indicates the probability that areas classified as that class on the map actually represents the class on the ground. For mangrove, producer's accuracy varied from 79 percent to 91 percent for the hyperspectral image and from 85 percent to 91 percent for the MNF image, and user's accuracy varied from 74 percent to 97 percent for the hyperspectral image and from 94 percent to 97 percent for the MNF image among the four methods for site 1 (Table 1). The MNF image produced better producer's and user's accuracies than the hyperspectral image based on minimum distance and SAM, and provided more consistent accuracies among the four classifiers. Among the eight classification maps, minimum distance applied to the MNF image had the best producer's and user's accuracies for identifying black mangrove at site 1, though maximum likelihood applied to the MNF image had higher overall accuracy and comparable producer's and user's accuracies for black mangrove.

Table 3 presents the error matrix and accuracy measures for the classification map generated from the 20-band MNF image based on maximum likelihood for site 1. Maximum likelihood had a producer's accuracy of 91 percent and a user's accuracy of 94 percent. One of the 33 black mangrove points verified on the ground was misclassified as bare soil and two of the 33 points as water (omission error). In addition, two of the 32 black mangrove points stratified in the classification map actually belonged to mixed vegetation (commission error). The omission error was mainly because the sparse black mangrove trees in the shallow water areas near the middle of the site were not effectively identified. The commission error was due to the fact that black mangrove had similar spectral response to mixed vegetation near the upper right corner of the site. Ideally, both producer's accuracy and user's accuracy should be high to accurately

TABLE 3. AN ERROR MATRIX AND ACCURACY MEASURES FOR A CLASSIFICATION MAP GENERATED FROM A 20-BAND MNF IMAGE FOR A MANGROVE SWAMP ON THE SOUTH TEXAS GULF COAST (SITE 1) BASED ON MAXIMUM LIKELIHOOD

	Actual category						
Classified category	Black mangrove	Mixed vegetation	Bare soil	Paved roads	Water	Total	User's accuracy
Mangrove	30	2	0	0	0	32	93.8%
Mixed vegetation	0	25	0	1	0	26	96.2%
Bare soil	1	1	27	0	0	29	93.1%
Paved roads	0	0	0	14	0	14	100.0%
Water	2	0	1	0	46	49	93.9%
Total	33	28	28	15	46	150	
Producer's accuracy	90.9%	89.3%	96.4%	93.3%	100.0%		

Overall accuracy = 94.7%. Overall kappa = 0.931. *Z*-statistic = 39.39.

identify the particular cover type. If one accuracy measure is high and the other is low, it is the lower accuracy value that determines how good the classification map is for that particular class. For example, the producer's accuracy was 85 percent and user's accuracy was 97 percent for the SAM-based classification map from the 20-band MNF image for site 1. Although 97 percent of the areas called black mangrove in the classification map were actually black mangrove, only 85 percent of the black mangrove areas in the image were correctly identified as black mangrove, indicating the classification map omitted 15 percent of the black mangrove areas on the ground.

For mixed vegetation, producer's and user's accuracies ranged from 61 percent to 96 percent for the hyperspectral image and from 89 percent to 96 percent for the MNF image (Table 1). All eight classifications performed well in separating mixed vegetation except that SAM applied to the hyperspectral image did not produce satisfactory results. For bare soil and paved roads, only minimum distance and SAM applied to the hyperspectral image had relatively lower accuracy values and the other six classifications had very good to excellent accuracy values. All eight classifications were able to identify water with accuracies from 87 percent to 100 percent. Again, the MNF image provided more consistent results than the hyperspectral image among the four classifiers for site 1.

Table 4 summarizes the accuracy assessment results for the classification maps generated from both the noise-reduced 214-band hyperspectral image and the 20-band MNF image based on the four classification methods for site 2. Overall accuracy ranged from 69 percent based on minimum distance to 91 percent based on Mahalanobis distance for the hyperspectral image and from 86 percent based on minimum distance to 91 percent based on maximum likelihood for the MNF image. Overall kappa varied from 0.63 to 0.89 for the hyperspectral image and from 0.83 to 0.89 for the MNF image among the four classifiers. All the classifications were significantly better than a random classification at the 95 percent confidence level. Table 5 presents *Z*-statistic values for making pairwise comparisons among the eight classifications for site 2. The minimum distance-based classification from the hyperspectral image was significantly worse than the other seven classifications, but there were no significant differences in overall accuracy among the seven classifications at the 95 percent confidence level.

For black mangrove identification, Mahalanobis distance applied to the hyperspectral image performed well, while the other three classifiers did not provide satisfactory results for site 2. However, all four classifiers applied to the MNF image were able to distinguish black mangrove with

TABLE 4. ACCURACY ASSESSMENT RESULTS FOR EIGHT CLASSIFICATION MAPS GENERATED FROM A NOISE-REDUCED 214-BAND HYPERSPECTRAL IMAGE AND ITS 20-BAND MNF IMAGE FOR A MANGROVE SWAMP ON THE SOUTH TEXAS GULF COAST (SITE 2)

				Producer's accuracy (PA, %) and user's accuracy (UA, %)											
Classification method	Overall accuracy (%)	Overall kappa	Z statistic	Black mangrove		Cattail		Mixed vegetation		Algae flats		Bare soil		Water	
				PA	UA	PA	UA	PA	UA	PA	UA	PA	UA	PA	UA
214-band hyperspectral image															
MD[a]	69.3	0.628	14.22*	66.7	34.8	33.3	63.6	51.4	66.7	77.8	51.9	78.6	88.0	97.2	94.6
MAHD	91.3	0.894	31.69*	100.0	92.3	90.5	95.0	82.9	87.9	88.9	84.2	96.4	87.1	94.4	100.0
ML	86.0	0.827	23.75*	41.7	100.0	90.5	95.0	80.0	75.7	77.8	82.4	100.0	77.8	97.2	100.0
SAM	84.7	0.812	22.85*	66.7	47.1	57.1	92.3	85.7	83.3	100.0	92.9	86.7	100.0	91.7	100.0
20-band MNF image															
MD	86.0	0.829	23.92*	91.7	78.6	90.5	90.5	68.6	77.4	94.4	77.3	89.3	89.3	91.7	97.1
MAHD	89.3	0.869	28.26*	83.3	83.3	95.2	83.3	89.7	77.1	85.0	94.4	90.0	96.4	97.1	97.2
ML	90.7	0.886	30.44*	91.7	91.7	90.5	95.0	77.1	87.1	94.4	81.0	96.4	87.1	97.2	100.0
SAM	87.3	0.846	25.80*	91.7	84.6	100.0	87.5	57.1	95.2	94.4	70.8	92.9	89.7	100.0	92.3

[a] MD = minimum distance, MAHD = Mahalanobis distance, ML = maximum likelihood, and SAM = spectral angle mapper.

* Significantly different from a random classification at the 0.05 level. The critical value $Z_{0.025}$ is 1.96.

TABLE 5. KAPPA ANALYSIS RESULTS (Z-STATISTIC) FOR PAIRWISE COMPARISONS AMONG EIGHT CLASSIFICATION MAPS GENERATED FROM A NOISE-REDUCED 214-BAND HYPERSPECTRAL IMAGE AND ITS 20-BAND MNF IMAGE FOR A MANGROVE SWAMP ON THE SOUTH TEXAS GULF COAST (SITE 2)

	Based on 214-band hyperspectral image				Based on 20-band MNF image		
Classification method	MD	MAHD	ML	SAM	MD	MAHD	ML
214-band hyperspectral image							
MAHD[a]	−5.08*						
ML	−3.54*	1.50					
SAM	−3.25*	1.80	0.29				
20-band MNF image							
MD	−3.59*	1.45	−0.05	−0.34			
MAHD	−4.49*	0.58	−0.92	−1.22	−0.88		
ML	−4.88*	0.20	−1.30	−1.60	−1.25	−0.38	
SAM	−3.97*	1.11	−0.40	−0.69	−0.35	0.53	0.91

[a] MD = minimum distance, MAHD = Mahalanobis distance, ML = maximum likelihood, and SAM = spectral angle mapper.

* Significantly different between the two classifications at the 0.05 level. The critical value $Z_{0.025}$ is 1.96. The negative sign indicates that the classification method on the top is worse than the one on the left.

good to excellent accuracies for the site. Among the eight classification maps, Mahalanobis distance applied to the hyperspectral image had the best producer's accuracy (100 percent) and user's accuracy (92 percent) for black mangrove, though maximum likelihood applied to the MNF image also provided excellent producer's and user's accuracies (both 92 percent). Table 6 presents the error matrix and accuracy measures for the classification map generated from the 20-band MNF image based on maximum likelihood for site 2. One of the 12 black mangrove points verified on the ground was misclassified as mixed vegetation (omission error) and one of the 12 black mangrove points stratified in the classification map actually belonged to mixed vegetation (commission error).

Mahalanobis distance and maximum likelihood applied to the hyperspectral image accurately identified cattail, but minimum distance and SAM were not able to separate the species from the hyperspectral image for site 2. In contrast, all four classifiers accurately distinguished cattail from the MNF image. For mixed vegetation, all methods except minimum distance produced satisfactory results from the hyperspectral image, but only Mahalanobis distance and maximum likelihood provided fair to good accuracies from the MNF image. For algae flats, all the classifications from both types of images produced satisfactory results except the minimum distance-based classification from the hyperspectral image. All the classifications were able to separate bare soil with producer's and user's accuracies ranging from 78 percent to 100 percent. Water was accurately identified in all eight classifications with accuracies from 92 percent to 100 percent.

Although there is no set standard for accuracy targets, a commonly recommended overall accuracy target is 85 percent with no class accuracy less than 70 percent (Thomlinson *et al.*, 1999; Foody, 2002). According to this guideline, the classification generated from the hyperspectral image based on SAM did not meet the overall and class accuracy targets for site 1. Although the classification generated from the hyperspectral image based on minimum distance met the overall target, it had user's accuracy of only 67 percent for bare soil at site 1. All other six classifications for site 1 met both the overall and class accuracy targets. For site 2, only three of the eight classifications met both the overall and class accuracy targets, including the Mahalanobis distance-based classifications from both types of images and the maximum likelihood-based classification from the MNF image.

Many remote sensing studies have been conducted for mapping mangrove wetlands in the world, but it is very difficult to compare the results from this study with other studies because of different environmental conditions. Nevertheless, this study can be compared with two other studies conducted in the south Texas Gulf coast. Everitt

TABLE 6. AN ERROR MATRIX AND ACCURACY MEASURES FOR A CLASSIFICATION MAP GENERATED FROM A 20-BAND MNF IMAGE FOR A MANGROVE SWAMP ON THE SOUTH TEXAS GULF COAST (SITE 2) BASED ON MAXIMUM LIKELIHOOD

	Actual category							
Classified category	mangrove	Cattail	Mixed vegetation	Algae flats	Bare soil	Water	Total	User's accuracy
Mangrove	11	0	1	0	0	0	12	91.7%
cattail	0	19	1	0	0	0	20	95.0%
Mixed vegetation	1	2	27	0	1	0	31	87.1%
Algae flats	0	0	4	17	0	0	21	81.0%
Bare soil	0	0	2	1	27	1	31	87.1%
Water	0	0	0	0	0	35	35	100.0%
Total	12	21	35	18	28	36	150	
Producer's accuracy	91.7%	90.5%	77.1%	94.4%	96.4%	97.2%		

Overall accuracy = 90.7%. Overall kappa = 0.886. *Z*-statistic = 30.44.

et al. (1999) reported an overall accuracy of 82 percent and producer's and user's accuracies of 72 percent and 87 percent, respectively, for black mangrove based on one single classification of an airborne false-color video image along the south Texas Gulf coast. More recently, Everitt *et al.* (2007) evaluated aerial CIR photography and digital CIR imagery for mapping two mangrove swamps along the south Texas Gulf coast and obtained overall accuracy values of over 80 percent and class accuracy values of over 79 percent for black mangrove. The results based on the hyperspectral imagery in this study are comparable or better than those based on aerial photography and airborne multispectral imagery in these two earlier studies. Besides, the previous studies used either an unsupervised or a supervised classification technique on CIR photographs and digital CIR imagery. In comparison, this study employed the MNF transformation and four different classification techniques to airborne hyperspectral imagery. The large number of bands and different classification techniques allowed the best classification maps to be generated, thus obtaining optimal overall and class accuracies. Although a range of remote sensing techniques has been evaluated to map mangroves at different regions in the world, there is no single best type of imagery or image processing technique that can be applied in every situation. The types of imagery and image processing techniques to be employed depend on a variety of factors such as size of the study area, complexity of associated plant communities, and time and cost restrictions.

Conclusions

This study demonstrates how image transformation and classification techniques can be applied to airborne hyperspectral imagery for mapping black mangrove distributions along the south Texas Gulf coast. MNF transformation applied to hyperspectral imagery can significantly reduce the number of bands needed for image classification. The transformed imagery with spatially coherent MNF bands in this study was effective for distinguishing black mangrove from associated plant species and other cover types. Although the inversely transformed or noise-reduced imagery contained the same number of bands as the original data, it was also effective for identifying black mangrove. However, MNF imagery requires less computing resources, and therefore it is a preferable approach to use MNF imagery for classification, especially if large numbers of hyperspectral images are to be classified. Moreover, the MNF imagery in this study provided similar or better classification results compared with the hyperspectral imagery. It also provided more consistent classification results than the noise-reduced hyperspectral imagery among the four classifiers.

Among the four classification methods examined in this study, maximum likelihood provided excellent overall accuracy as well as excellent producer's and user's accuracies for black mangrove for both sites based on the MNF imagery, though some of the classifiers also provided excellent results for site 1 or site 2. Classification results depend on the composition of plant species and the growth conditions at a specific site, and the best classification methods identified for one site may not perform the best for other sites. Nevertheless, the procedures presented in this study can be useful for monitoring and mapping mangrove swamps in other coastal environments. With the advancement in computing and image processing techniques, it is always necessary to evaluate different image processing and classification techniques in order to obtain the best classification results, especially when hyperspectral imagery is used. This study was one of the few evaluations of airborne hyperspectral imagery for mapping black mangrove and the first one on the south Texas Gulf coast. More research is needed to evaluate airborne hyperspectral imagery and compare it with other types of imagery for mapping mangrove wetlands.

Acknowledgments

The authors thank Rene Davis (USDA-ARS, Weslaco, TX) for acquiring the hyperspectral imagery; and Jim Forward and Fred Gomez (USDA-ARS, Weslaco, TX) for assistance in image rectification and ground accuracy assessment.

References

Amarasinghe, M.D., and S. Balasubramaniam, 1992. Net primary productivity of two mangrove forest stands on the northwestern coast of Sri Lanka, *Hydrobiologia*, 241:31–41.

Aschbacher, J., R. Ofren, J.P. Delsol, T.B. Suselo, S. Vibulsresth, and T. Charrupat, 1995. An integrated comparative approach to mangrove vegetation mapping using advanced remote sensing and GIS technologies: Preliminary results, *Hydrobiologia*, 295:285–294.

Boardman, J.W., and F.A. Kruse, 1994. Automated spectral analysis: A geologic example using AVIRIS data, north Grapevine Mountains, Nevada, *Proceedings of the Tenth Thematic Conference on Geologic Remote Sensing*, Environmental Research Institute of Michigan, Ann Arbor, Michigan, pp. I407–I418.

Chauvaud, S., C. Bouchon, and R. Maniere, 1998. Remote sensing techniques adapted to high resolution mapping of tropical coastal marine ecosystems (coral reefs, seagrass beds and mangrove), *International Journal of Remote Sensing*, 19(18):3625–3639.

Campbell, J.B., 2002. *Introduction to Remote Sensing*, Third edition, The Guilford Press, New York.

Congalton, R.G., and K. Green, 1999. *Assessing the Accuracy of Remotely Sensed Data: Principles and Practices*, Lewis Publishers, Boca Raton, Florida.

Day, J.W. Jr., C. Coronado-Molina, F.R. Vera-Herrera, R. Twilley, V.H. Rivera-Monroy, H. Alvarez-Guillen, R. Day, and W. Conner, 1996. A 7 year record of above-ground net primary production in a southeastern Mexican mangrove forest, *Aquatic Botany*, 55:39–60.

Day, J.W. Jr., W.H. Conner, F. Ley-lou, R.H. Day, and A.M. Navarro, 1987. The productivity and composition of mangrove forests, Laguna de Terminos, Mexico, *Aquatic Botany*, 27:267–284.

Environmental Protection Agency (EPA), 2006. Mangrove swamps, *http://www.epa.gov/owow/wetlands/types/mangrove.html*, EPA Water Resource Center, Washington, D.C. (last date accessed: 14 January 2009).

ERDAS, 2002, *ERDAS Field Guide*. ERDAS, LLC., Atlanta, Georgia.

Everitt, J.H., and F.W. Judd, 1989. Using remote sensing techniques to distinguish and monitor black mangrove (*Avicennia germinans*), *Journal of Coastal Research*, 5:737–745.

Everitt, J.H., D.E. Escobar, and F.W. Judd, 1991. Evaluation of airborne video imagery for distinguishing black mangrove (*Avicennia germinans*) on the lower Texas gulf coast, *Journal of Coastal Research*, 7:1169–1173.

Everitt, J.H., D.E. Escobar, C. Yang, R.I. Lonard, F.W. Judd, M.A. Alaniz, I. Cavazos, M.R. Davis, and D.L. Hockaday, 1999. Distinguishing ecological parameters in a coastal area using a video system with visible/near-infrared/mid-infrared sensitivity, *Journal of Coastal Research*, 15:1145–1150.

Everitt, J.H., C. Yang, K.R. Summy, F.W. Judd, and M.R. Davis, 2007. Evaluation of color-infrared photography and digital imagery to map black mangrove on the Texas Gulf coast, *Journal of Coastal Research*, 15:1145–1150.

Foody, G.M., 2002. Status of land cover classification accuracy assessment, *Remote Sensing of Environment*, 80(1):185–201.

Gang, P., and J.L. Agatsiva, 1992. The current status of mangroves along the Kenyan coast: A case study of Mida Creek mangroves based on remote sensing, *Hydrobiologia*, 247:29–36.

Gao, J., 1999. A comparative study on spatial and spectral resolutions of satellite data in mapping mangrove forests, *International Journal of Remote Sensing*, 20(14):2823–2833.

Green, E.P., C.D. Clark, P.J. Mumby, and A.C. Ellis, 1998. Remote sensing techniques for mangrove mapping, *International Journal of Remote Sensing*, 19:935–956.

Green, A.A., M. Berman, P. Switzer, and M.D. Craig, 1988. A transformation for ordering multispectral data in terms of image quality with implications for noise removal, *IEEE Transactions on Geoscience and Remote Sensing*, 26(1):65–74.

Held, A., C. Ticehurst, L. Lymburner, and N. Williams, 2003. High resolution mapping of tropical mangrove ecosystems using hyperspectral and radar remote sensing, *International Journal of Remote Sensing* 24(13):2739–2759.

Hirano, A., M. Madden, and R. Welch, 2003. Hyperspectral image data for mapping wetland vegetation, *Wetlands*, 23(2):436–448.

Jensen, J.R., H. Lin, X. Yang, E.W. Ramsey III, B.A. Davis, C.W. Thoemke, 1991. The measurement of mangrove characteristics in southwest Florida using SPOT multispectral data, *Geocarto International*, 2:13–21.

Kairo, J.G., B. Kivyatu, and N. Koedam, 2002. Application of remote sensing and GIS in the management of mangrove forests within and adjacent to Kiunga Marine Protected Area, Lamu, Kenya, *Environment, Development and Sustainability*, 4:153–166.

Kruse, F.A., A.B. Lefkoff, J.B. Boardman, K.B. Heidebrecht, A.T. Shapiro, P.J. Barloon, and A.F.H. Goetz, 1993. The Spectral Image Processing System (SIPS) - Interactive visualization and analysis of imaging spectrometer data, *Remote Sensing of Environment*, 44:145–163.

Kumar, P.K.D., G. Gopinath, C.M. Laluraj, P. Seralathan, and D. Mitra, 2007. Change detection studies of Sagar Island, India, using Indian Remote Sensing Satellite 1C Linear Imaging Self-Scan Sensor III Data, *Journal of Coastal Research*, 23(6):1498–1502.

Long, B.G., and T.D. Skewes, 1996. A technique for mapping mangroves with Landsat TM satellite data and geographic information system, *Estuarine, Coastal and Shelf Science*, 43:373–381.

Manson, F.J., N.R. Loneragan, and S.R. Phinn, 2003. Spatial and temporal variation in distribution of mangroves in Moreton Bay, subtropical Australia: A comparison of pattern metrics and change detection analyses based on aerial photographs, *Estuarine, Coastal and Shelf Science*, 57:653–666.

Mao, L., Y. Zhang, and H. Bi, 2006. Modern pollen deposits in coastal mangrove swamps from northern Hainan Island, China, *Journal of Coastal Research*, 22(6):1423–1436.

Marshall, N., 1994. Mangrove conservation in relation to overall environmental consideration, *Hydrobiologia*, 285:303–309.

Mougin, E., C. Proisy, G. Marty, F. Fromard, H. Puig, J.L. Betoulle, and J.P. Rudant, 1999. Multifrequency and multipolarization radar backscattering from mangrove forests, *IEEE Transactions on Geoscience and Remote Sensing*, 37(1):94–102.

Pasqualini, V., J. Iltis, N. Dessay, M. Lointier, O. Guelorget, and L. Polidori, 1999. Mangrove mapping in North-Western Madagascar using SPOT-XS and SIR-C radar data, *Hydrobiologia*, 413:127–133.

Primavera, J.H., 1997. Fish predation on mangrove-associated penaeids - The role of structures and substrate, *Journal of Experimental Marine Biology and Ecology*, 215:205–216.

Proisy, C., P. Couteron, and F. Fromard, 2007. Predicting and mapping mangrove biomass from canopy grain analysis using Fourier-based textural ordination of IKONOS images, *Remote Sensing of Environment*, 109:379–392.

Ramasubramanian, R., L. Gnanappazham, T. Ravishankar, and M. Navamuniyammal, 2006. Mangroves of Godavari - Analysis through remote sensing approach, *Wetlands Ecology and Management*, 14:29–37.

Ramsey, E.W. III, and J.R. Jensen, 1996. Remote sensing of mangrove wetlands: Relating canopy spectra to site-specific data, *Photogrammetric Engineering & Remote Sensing*, 62(9):939–948.

Richards, J.A., 1999. *Remote Sensing Digital Image Analysis*, Springer-Verlag, Berlin, 240 p.

Saito, H., M.F. Bellan, A. Al-Habshi, M. Aizpuru, F. Blasco, 2003. Mangrove research and coastal ecosystem studies with SPOT-4 HRVIR and TERRA ASTER in the Arabian Gulf, *International Journal of Remote Sensing*, 24(21):4073–4092.

Sasekumar, A, V.C. Chong, M.U. Leh, and R. D'Cruz, 1992. Mangroves as a habitat for fish prawns, *Hydrobiologia*, 247:195–207.

Tam, N.F.Y., Y.S. Wong, 1999. Mangrove soils in removing pollutants from municipal wastewater of different salinities, *Journal of Environmental Quality*, 28:556–564.

Thomlinson, J.R., P.V. Bolstad, and W.B. Cohen, 1999. Coordinating methodologies for scaling landcover classifications from site-specific to global: Steps toward validating global map products, *Remote Sensing of Environment*, 70(1):16–28.

Vaiphasa, C, W.F. de Boer, A.K. Skidmore, S. Panitchart, T. Vaiphasa, N. Bamrongrugsa, and P. Santitamnont, 2007. Impact of solid shrimp pond waste materials on mangrove growth and mortality: A case study from Pak Phanang, Thailand, *Hydrobiologia*, 591:47–57.

Vaiphasa, C., S. Ongsomwang, T. Vaiphasa, and A.K. Skidmore, 2005. Tropical mangrove species discrimination using hyperspectral data: A laboratory study, *Estuarine, Coastal and Shelf Science*, 65:371–379.

Vaiphasa C, A.K. Skidmore, W.F. de Boer, 2006. A post-classifier for mangrove mapping using ecological data, *ISPRS Journal of Photogrammetry and Remote Sensing*, 61:1–10.

Valiela, I., J.L. Bowen, and J.K. York, 2001. Mangrove forests: One of the world's threatened major tropical environments, *BioScience*, 51(10):807–815.

Wang, L., W.P. Sousa, and P. Gong, 2004a. Integration of object-based and pixel-based classification for mapping mangroves with IKONOS imagery, *International Journal of Remote Sensing*, 25(24):5655–5668.

Wang, L., W.P. Sousa, P. Gong, and G.S. Biging, 2004b. Comparison of IKONOS and QuickBird images for mapping mangrove species on the Caribbean coast of Panama, *Remote Sensing of Environment*, 91:432–440.